AUTHOR(S):

Nakao, Megumi; Kobayashi, Kotaro; Tokuno, Junko; Chen-Yoshikawa, Toyofumi; Date, Hiroshi; Matsuda, Tetsuya

京都大学
KYOTO UNIVERSITY

KURENAI 紅
Kyoto University Research Information Repository

Research paper

Deformation analysis of surface and bronchial structures in intraoperative pneumothorax using deformable mesh registration

Megumi Nakao [a,*], Kotaro Kobayashi [a], Junko Tokuno [b], Toyofumi Chen-Yoshikawa [c], Hiroshi Date [b], Tetsuya Matsuda [a]

[a] Graduate School of Informatics, Kyoto University, Yoshida-Honmachi, Sakyo, Kyoto, 606–8501, Japan
[b] Kyoto University Hospital, 54 Kawaharacho, Shogoin, Sakyo, Kyoto, 606–8507, Japan
[c] Nagoya University Hospital, 65 Tsurumai-cho, Showa-ku, Nagoya, 466–8550, Japan

ARTICLE INFO

ABSTRACT

The positions of nodules can change because of intraoperative lung deflation, and the modeling of pneumothorax-associated deformation remains a challenging issue for intraoperative tumor localization. In this study, we introduce spatial and geometric analysis methods for inflated/deflated lungs and discuss heterogeneity in pneumothorax-associated lung deformation. Contrast-enhanced CT images simulating intraoperative conditions were acquired from live Beagle dogs. The images contain the overall shape of the lungs, including all lobes and internal bronchial structures, and were analyzed to provide a statistical deformation model that could be used as prior knowledge to predict pneumothorax. To address the difficulties of mapping pneumothorax CT images with topological changes and CT intensity shifts, we designed deformable mesh registration techniques for mixed data structures including the lobe surfaces and the bronchial centerlines. Three global-to-local registration steps were performed under the constraint that the deformation was spatially continuous and smooth, while matching visible bronchial tree structures as much as possible. The developed framework achieved stable registration with a Hausdorff distance of less than 1 mm and a target registration error of less than 5 mm, and visualized deformation fields that demonstrate per-lobe contractions and rotations with high variability between subjects. The deformation analysis results show that the strain of lung parenchyma was 35% higher than that of bronchi, and that deformation in the deflated lung is heterogeneous.

1. Introduction

Recent advances in medical imaging devices have increased the chances of finding early-stage cancer, metastatic lung tumors, and benign nodules. Although the positions of lung nodules can be identified preoperatively on computed tomography (CT) images, the lungs deform or collapse during surgery, which prevents accurate tumor localization and increases the difficulty of resection procedures. In the last decade, image-based and model-based intraoperative guidance have been explored in laparoscopic surgery (Koo et al., 2017; Heiselman et al., 2018); however, pneumothorax-associated lung deformation has not been targeted because of a lack of clinical datasets and the complex properties of lung tissue. The analysis and modeling of pneumothorax-associated deformation and its application to intraoperative tumor localization therefore remains a challenging area of research for biomedical engineering.

In the image-based analysis of lung modeling, respiratory motion has been extensively investigated (Ehrhardt et al., 2011; Sadeghi-Naini et al., 2012; Ilegbusi et al., 2012; Fuerst et al., 2015; Wilms et al., 2016; Jud et al., 2017). However, because of difficulties in both image registration and regularization, few studies have modelled the pneumothorax-associated deformation that can occur between the preoperative and intraoperative lung states. When deformable registration is applied to CT images of pneumothorax, two technical issues should be addressed: the CT intensity shift and the major deformation with both rotational and topological changes. The CT intensity shift derives from the atelectasis state, in which there are variations in air content within the lungs; this changes pixel values and severely lowers image contrast, seriously impairing image-based registration. Lungs are very soft and their deformation is accompanied by significant volume reduction inside the thoracic cavity, which results in topological changes in the CT

* Corresponding author.: Fax: +81 75 753 3375.
  E-mail address: megumi@i.kyoto-u.ac.jp (M. Nakao).

A Self-archived copy in
Kyoto University Research Information Repository
https://repository.kulib.kyoto-u.ac.jp

京都大学学術情報リポジトリ
KURENAI 紅
Kyoto University Research Information Repository

image space. The mechanism of pneumothorax-associated lung deformation is complex and not mathematically understood, except through simulation studies of animal lungs (Sadeghi-Naini et al., 2012; Naini et al., 2011).

Deformable image registration techniques (Sotiras et al., 2013; Oh and Kim, 2017; Klein et al., 2010; Beg et al., 2005) have been used for numerical analyses of organ and soft tissue deformation. Intraoperative deformation derived from changes in internal pressure, patient posture, and tool manipulation has been studied in respect to intraoperative guidance systems (Kenngott et al., 2014; Wagner et al., 2016; Nickel et al., 2018; Koo et al., 2017; Rühaak et al., 2017; Nakao and Minato, 2010; Gunay et al., 2016; Tokuno et al., 2020), and studies have reported results of deformable registration designed for guidance of thoracoscopic surgery. Uneri et al. presented a deformable registration framework for pneumothorax cone beam CT (CBCT) images of animal lungs (Uneri et al., 2013), and an integrated framework of model-based and image-based registration was used to address CT intensity shifts; however, the limited field of view of CBCT is its major limitation for deformation analysis and the main focus of the work was registration of bronchial junctions. Alvarez et al. analyzed CBCT images of lungs deformed because of posture differences (Alvarez et al., 2018), and Nakao et al. designed a deformable mesh registration (DMR) framework for registering pneumothorax-associated lung shapes and statistically investigated lung surface deformation in animal CT datasets (Nakao et al., 2019). More recently, the deflated lung surfaces of patients with pneumothorax were evaluated using hyperelastic finite-element models (Lesage et al., 2020). However, to the best of our knowledge, no study has reported registration results for the overall shape of the lungs including all lobes and internal bronchial structures, nor analyzed their spatial displacements. Therefore, we performed data acquisition and detailed numerical analysis with the aim of generating a statistical formulation of pneumothorax-associated deformation.

The purpose of this study was to perform a spatial and geometric analysis of pneumothorax-associated lung deformation to better understand the intraoperative state of the lung. Specifically, we sought to determine the heterogeneity of 3D displacements as evidenced by targeting of the lung's surface, parenchyma and bronchial tree structures. In this analysis, we used pairs of contrast-enhanced CT datasets acquired at two bronchial pressures (designated as inflated and deflated states) from 11 live Beagle dogs. To address the difficulties of mapping pneumothorax CT images with topological changes and CT intensity shifts, we designed a DMR framework for mixed data structures including the lobe surfaces and bronchial centerlines. We used the spatial maps obtained from the inflated/deflated lungs to investigate differences in strain (a measure of the displacement between particles in the body relative to a reference length) on the lung's parenchyma and bronchial tree structures.

The contributions of this paper are summarized as follows.

- a complete deformable mesh registration solution for mapping inflated/deflated lungs with topological changes
- a mapping function design for mixed data structures of the lobe surfaces and the bronchial tree structures with incomplete correspondence derived from CT intensity shifts
- visualization of deformation fields that demonstrate per-lobe contractions and rotations with high variability between subjects
- numerical analysis of heterogeneity in pneumothorax-associated deformation of whole lungs

The registered models and findings can be directly used for statistical modeling of lung deflation. The potential clinical applications include localization of deep tumors or nodules and development of intraoperative visual guidance for thoracoscopic surgery.

2. Methods

2.1. Measurements and preprocessing

To analyze spatial displacements in collapsed lungs, we used CT images acquired from 11 live Beagle dogs. These datasets were acquired in a previous study for the purpose of simulating intraoperative conditions and analyzing surface deformation (Nakao et al., 2019). In this paper, we briefly describe the imaging process and conditions. Contrast-enhanced CT images were measured from the left lungs at two bronchial pressures (14 and 2 cmH$_2$O) at the Institute of Laboratory Animals, Kyoto University. This study was performed in accordance with the regulations of the Animal Research Ethics Committee of Kyoto University. All CT images were acquired with a 16-row multidetector CT scanner (Alexion 16; Toshiba Medical Systems, Tochigi, Japan). The dogs were administered ketamine, xylazine, and rocuronium before undergoing tracheal intubation and mechanical ventilation with a ventilator (Savina 300; Drager AG & Co. KGaA, LüBeck, Germany). Using the ventilator, bronchial pressure was set to 14 cmH$_2$O to obtain images of fully expanded lungs (inflated state) and to 2 cmH$_2$O for imaging of collapsed lungs (deflated state). All dogs were placed in a right lateral (decubitus) position on the bed of the CT scanner, and CT images were acquired in the inflated and deflated states.

Fig. 1 shows CT slice images and volume rendered results of bronchial tree structures in the inflated and deflated states after rigid registration of the two volumes using the spine and bed as fixed references. The window width and level were set to 700 HU and −600 HU, respectively. The CT intensity values changed because of differences in the air content of the lung, with the image contrast in the deflated state becoming significantly lower than that in the inflated state. With this intensity shift, the CT values of the parenchyma increase (the parenchyma region becomes brighter), as can be seen in Fig. 1 (a). A large space outside of the lung because of air flowing into the thoracic cavity in the deflated state is also confirmed. The accuracy of image-based registration can be affected by these image characteristics, and we found that some image-based registration algorithms failed, having large registration errors in the edge of the deformed lung surfaces. Therefore, analysis of the pneumothorax-associated lung deformation requires a stable registration framework that addresses the intensity shifts and major deformations with topological changes inside the thoracic cavity.

Fig. 1 (b) show the segmented bronchial labels in the inflated/deflated states, with red and green arrows showing the es-
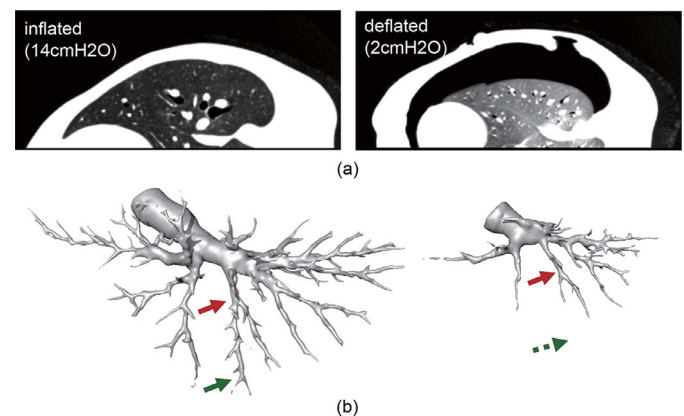

Fig. 1. CT slice images and extracted bronchial structures in the inflated/deflated states. (a) Intensity shift and topological changes inside the thoracic cavity, and (b) the paired bronchial labels extracted using the same CT values. (Arrows indicate estimated corresponding points).

京都大学
KYOTO UNIVERSITY

M. Nakao, K. Kobayashi, J. Tokuno et al.

Medical Image Analysis 73 (2021) 102181

KURENAI 紅
京都大学学術情報リポジトリ
Kyoto University Research Information Repository

Table 1

Specifications of the paired lung geometry datasets in inflated/deflated states. V_u: volume of upper lobe, V_l: volume of lower lobe, N_j: number of bronchial junctions, and N_e: number of bronchial terminals.

Case	inflated state				deflated state			
	V_u [cc]	V_l [cc]	N_j	N_e	V_u [cc]	V_l [cc]	N_j	N_e
1	173.5	242.9	58	62	82.7	96.9	44	48
2	167.1	508.3	63	64	69.9	116.4	62	63
3	231.7	357.6	66	67	111.4	145.3	40	48
4	184.7	258.2	73	75	71.4	100.4	36	40
5	246.1	353.3	62	67	78.9	92.8	49	57
6	188.4	373.2	77	83	65.8	104.1	30	37
7	131.9	257.9	97	98	55.8	110.7	31	32
8	164.3	342.1	69	75	102.3	196.7	39	42
9	198.8	375.4	58	67	84.9	111.8	43	51
10	232.5	355.7	90	98	113.5	186.4	60	64
11	163.7	212.1	-	-	160.2	236.6	-	-
mean±SD	189.3±35.1	330.6±83.4	71.3±13.3	75.6±13.3	90.6±29.7	136.2±48.7	43.4±10.9	48.2±10.8

timated positions of corresponding points. Although both datasets were extracted using the same CT value threshold, there are clearly missing shapes around the bronchial terminals in Fig. 1 (b). As the inflated state shows the clear contrast of the bronchus because of the high air content, the finer structures can be extracted. On the other hand, the estimated bronchial terminal in the deflated state indicated by the dotted green arrow is not detected because of the intensity shift, and the bronchus is therefore visualized as being shorter than the estimated contraction. This means that deformable registration based on only bronchial structures results in incorrect matching results. To overcome the difficulty in matching two shapes with incomplete correspondence, we designed our mesh-based registration methods on the basis of surface and bronchial geometry.

Anatomical segmentation of the upper/lower lobes and bronchial structures was automatically performed using a Synapse VINCENT 3D medical image analysis system (Fujifilm, Tokyo, Japan). Tetrahedral meshes representing the lobes were independently created using Poisson surface reconstruction (Kazhdan et al., 2006) and tetrahedralization (See Figure 2). All models were resampled to 500 triangles while considering the surface representation and computational cost for DMR, resulting in 650–750 tetrahedra for each lobe. The bronchial labels were converted to centerlines using the Vascular Modeling Toolkit (VMTK) (Antiga and Steinman, 2011). Figure 2 (b) and (c) show the bronchial centerlines of inflated and deflated states, respectively. The centerlines comprised a tree structure with multiple nodes, including junctions and terminals. The root node represents the pulmonary hilum. Table 1 summarizes the specifications of the 11 paired lung models in the inflated and deflated states. V_u and V_l are the volumes of the upper and lower lobes, respectively. N_j is the number of bronchial junctions, and N_e is the number of bronchial terminals. These numbers are determined in VMTK based on the complexity of the centerline structures, with the deflated models showing smaller values. We note that in Case 11, the volume at a bronchial pressure of 2 cmH$_2$O showed an unexpected increase, which was probably a result of the bronchial pressure not being successfully controlled. Therefore, Case 11 was removed from our analyses.

2.2. Problem definition

The focus of this study was to investigate the spatial displacements of whole lungs, including their surfaces and bronchial structures. The displacement of bronchi can be partially obtained by matching anatomical feature points extracted from bronchial junctions (Nakamoto et al., 2007; Uneri et al., 2013). However, such landmark-based matching cannot be applied to the lung's curved surfaces because of their lack of anatomical features. DMR is increasingly being applied in practice because registered mesh models are directly available for statistical modeling and variational analysis (Ehrhardt et al., 2011; Kim et al., 2015; Jud et al., 2017). In addition, for anatomical structures with large shape variations, recent DMR methods (Kim et al., 2015; Nakao et al., 2019) have shown better registration accuracy than large-deformation diffeomorphic metric mapping (Beg et al., 2005).

The pair of lung mesh models representing the inflated and deflated states differed in the number of vertices and the data structure (i.e., tree and mesh topology) because they were independently generated from different CT images. In this study, the shape model M_I generated from the inflated lung is deformed to the deflated model M_D. We aimed to compute the registered model $\phi(M_I)$ (ϕ: mapping function) that precisely approximated the target surfaces and centerlines by DMR. Because the initial and registered model $(M_I, \phi(M_I))$ have the same data structure with point-to-point correspondence, the spatial deformation u can be obtained by calculating the displacement vectors of the corresponding vertices.

We performed a preliminary experiment to investigate the linearity of displacement in the lung lobes. We applied conventional DMR (Nakao et al., 2019) to the two lung surfaces of the inflated/deflated states and mapped the vertex displacement of the deformed tetrahedral mesh to all the nodes of the bronchial tree structures. This mapping involved a combination of DMR and spatial linear interpolation of the inside of the lobe surfaces and was implemented using the barycentric coordinates of the tetrahedral elements. Fig. 2 (e) shows the DMR result with linearly-mapped bronchial centerlines (blue) and the target centerlines in the deflated state (red).

If the pneumothorax-associated deformation is spatially homogeneous, the deformed bronchial centerline would coincide with the target centerline in the deflated state. However, as shown in Fig. 2(e), local mismatches of the bronchial junctions were found, as indicated by the arrows. Most of the datasets showed large deviations between the target and linearly mapped centerlines, suggesting that the displacement of the lung region was not spatially homogeneous. This preliminary analysis also shows that the pneumothorax-associated deformation is spatially continuous in each lobe, although some cases show irregular rotations between the upper and lower lobes. Based on the features observed between the lung surface and the bronchi, we designed the DMR framework by considering the following two issues.

- The lung surface and bronchial centerlines should be registered under the constraint that the deformation is spatially continuous and smooth while matching visible junctions as much as possible.
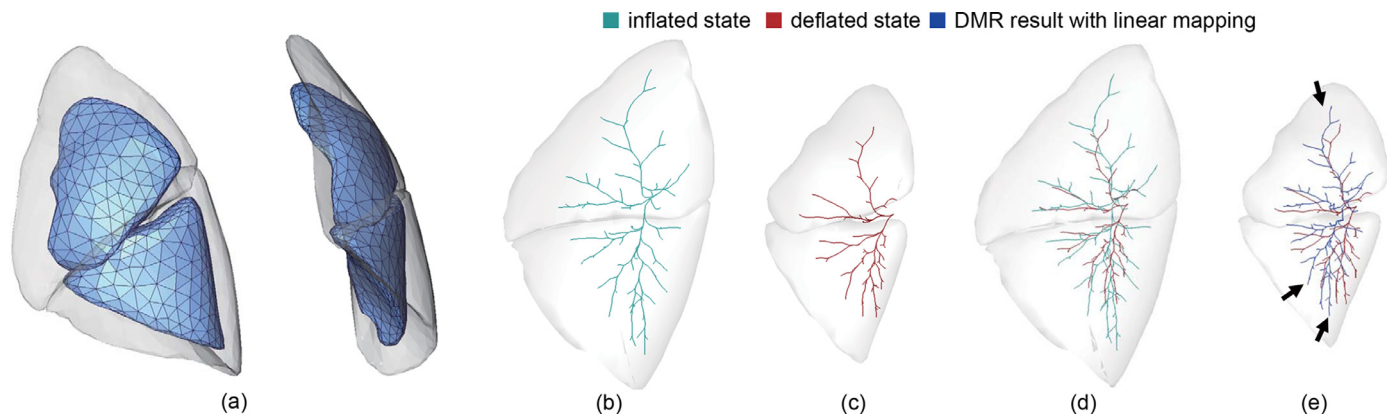
■ inflated state ■ deflated state ■ DMR result with linear mapping

(a)   (b)   (c)   (d)   (e)

Fig. 2. A typical example of the mesh models and DMR results. (a) Tetrahedral meshes in the inflated (translucent) and deflated states (opaque), (b) bronchial centerlines in the inflated state, (c) bronchial centerlines in the deflated state, (d) overlapping images and (e) deformed centerlines (blue) using conventional DMR and linear mapping. (For interpretation of the references to colour in this figure legend, the reader is referred to the web version of this article.)
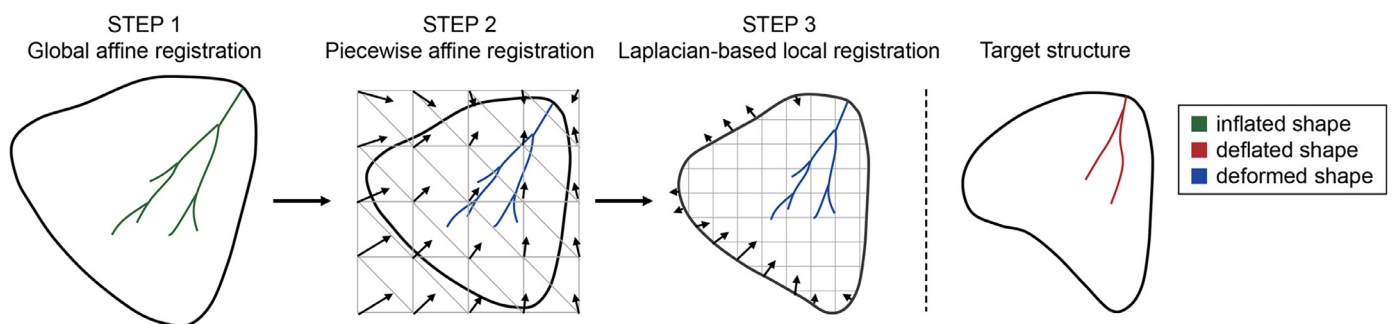

STEP 1
Global affine registration

STEP 2
Piecewise affine registration

STEP 3
Laplacian-based local registration

Target structure

■ inflated shape
■ deflated shape
■ deformed shape

Fig. 3. Proposed three-step DMR framework for mixed data structures with lung surfaces and centerlines. The registration process is applied to each lobe independently to cope with rotational components or sliding motion of pneumothorax-associated deformation.

- To handle the different rotations between the upper and lower lobes, mapping functions ϕ for deformable registration should be determined independently for each lobe.

2.3. DMR For lung surface and bronchial structures

Based on the problem definition, this section describes the outline of the DMR framework that matches the inflated and deflated lung models. The proposed DMR is designed to obtain non-linear mapping under the condition that the deformation field for the lung surface and bronchi is spatially continuous and smooth. The registration framework comprises the following three-step processes (See Fig. 3).

1. STEP 1 Global affine transformation
   Global registration is first applied to the inflated (source) model $M_I = (S_I, C_I)$ (S_I: the lung surface and C_I: the bronchial centerline in the inflated state) to roughly match it to the deflated (target) model $M_D = (S_D, C_D)$ (S_D: the lung surface and C_D: the bronchial centerline in the deflated state). In this step, a set of vertices of the lung surface and bronchial centerlines are transformed using $v'_i = Tv_i$ (T: transformation matrix, v_i: vertex position). As the root node of the bronchial tree structure represents the pulmonary hilum in our data, its position is used as the origin for normalizing the translation.

2. STEP 2 Piecewise affine (PWA) deformable registration
   The purpose of the next step is to locally register the surface and bronchial centerline while spatially deforming the entire lung region continuously and smoothly. A cuboid grid $\mathcal{M}$ formed by tetrahedral elements is first generated as the bounding box of the lung model $\phi(M_I)$ obtained in STEP 1. Here, The deformation field is discretely represented by per-vertex dis-

placement vectors of the cuboid grid, as shown by the arrows in Fig. 3. The vertex positions are updated while maintaining the connectivity between the vertices. The displacement of each vertex of the grid is mapped to all the surface and centerline vertices. The vertex displacements of the cuboid grid are obtained by minimizing an objective function. We introduce the objective function that addresses local mismatches on the missing parts of the bronchi while handling the mixed data structures with surface meshes and centerlines. The details are described in the next section.

3. STEP 3 Laplacian-based local mesh registration
   The final step is performed to improve registration results for the local shapes with large matching errors. The lung surface is refined based on the Laplacian-based diffeomorphic shape matching (LDSM) algorithm (Nakao et al., 2021b), and the deformation is mapped to the centerlines. Using a discrete Laplacian of the lung surface as the shape descriptor, LDSM achieves stricter surface matching while preserving the entire shape of the lung. Details of the LDSM algorithm and its registration performance for abdominal organs are reported in (Nakao et al., 2021b).

We applied the above registration process independently to each lobe to cope with rotation and sliding motion of the upper and lower lobes. Hence, the transformation matrix T for global affine transformation and mapping functions ϕ (i.e., deformation field u) for deformable registration was calculated for each lobe, and simultaneously updated per iteration in the registration process. For the propagation of deformation fields to the surface and bronchial structures, the barycentric coordinates of the vertices with regard to the corresponding tetrahedral element were calcu-
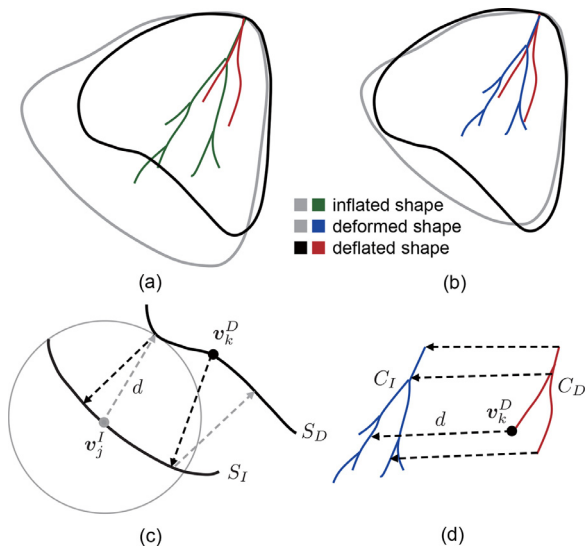
Fig. 4. Local distance measures for lung surfaces and bronchial centerlines with missing parts. (a) initial setup of the inflated and deflated models, (b) deformed and deflated models after global affine transformation, (c) bidirectional surface distance, and (d) one-way centerline distance.

lated in advance. All vertices were updated while keeping the relative position of the four points of the tetrahedral element.

2.4. Objective function

In STEP 1 and 2, the registered models are computed by minimizing the proposed objective function, which is designed to obtain a spatially continuous and smooth mapping of the lung surface and bronchial centerlines. The objective function is described as follows.

$$E = d(M_D, \phi(M_I)) + \int_0^1 \|L(u(s))\|^2 ds, \qquad (1)$$

where d is the distance function between the two models. $\phi(\cdot)$ is a continuous and differentiable transformation that maps the source model to the deformed model. $L(\cdot)$ is the Laplace–Beltrami operator and $L(u)$ is the discrete Laplacian of the deformation field \boldmath u.

The first term evaluates the difference between the deformed model and the target model, whereas the second is a regularization term to make the deformation field smooth. Figs 4 (a) and (b) illustrate examples of initial setups in Steps 1 and 2, respectively. To obtain accurate deformation fields that match the pneumothorax lung models with partial defects, we introduce the following distance measures.

Surface distance

The surface distance d_s is a loss function that evaluates the difference between the two curved surfaces. In this study, the distance between the source and target surfaces (S_I, S_D) is defined as follows:

$$d_s(S_I, S_D) = \sum_{v_j^I \in S_I} d(v_j^I, S_D)/N_I + \sum_{v_k^D \in S_D} d(v_k^D, S_I)/N_D, \qquad (2)$$

where S_I and S_D are the set of vertices for the inflated and deflated lung surfaces, respectively, and N_I and N_D are their number of vertices. Although the source surface is iteratively updated in the registration process, we use S_I for its notation, for readability purposes. v_j^I represents the 3D position of the j-th vertex of S_I, and v_j^I is the 3D position of the k-th vertex of S_D. m and n are the

numbers of vertices for S_I and S_D, respectively. $d(v, V)$ is the minimum point distance between a vertex v and a set of vertices V of a curved surface, and is defined by

$$d(v, S) = |v - \hat{v}_p|$$
$$s.t. \quad \hat{v}_p = \min_{v_p} \{|v - v_p| + \gamma(1 - n \cdot n_p)\}, \qquad (3)$$

where γ is a weight, v_p is a vertex of the curved surfaces S, and n and n_p are vertex normals at v and v_p, respectively. To avoid matching errors around the ridges or tips of the lung surface, the closest point $\hat{v}_p$ from v is determined by considering the vertex normal. Figure 4(c) illustrates $d(v_j^I, S_D)$ (gray) and $d(v_k^D, S_I)$ (black). d_s is computed as the average of the bidirectional distances from the surface to the other surface and is available as a stable index even for highly frequent shape changes and noise. This error metric is also referred to as a mean distance and is used to evaluate registration accuracy (Kim et al., 2015; Nakao et al., 2019).

One-way centerline distance

The one-way centerline distance d_c is a loss function that evaluates the distance between the two centerlines (C_I, C_D) with incomplete correspondence. Unlike for the surface distance, we employ a one-way distance measure to consider the missing shapes of the deflated bronchi. Bidirectional distance is a well-established geometric error metric when two shapes (e.g., bronchial trees here) represent the same anatomical region. However, as shown in Fig. 1, the bronchial trees obtained from the pneumothorax CT images do not represent the same anatomical regions because most of the terminal shapes are not detected following the CT intensity shift. The bronchial tree in the deflated state C_D is visualized as being shorter than the estimated shape, even after consideration of lung deflation, and bronchial tree registration using bidirectional distance results in anatomically wrong matching around the terminal. The one-way centerline distance we used is described by

$$d_c(C_I, C_D) = \sum_{v_k^D \in C_D} d(v_k^D, C_I)/N_C, \qquad (4)$$

where C_I and C_D are the set of vertices for the bronchial centerlines in the inflated and deflated states, N_C is the number of vertices for C_D, $d(v, C)$ is the minimum point distance between a vertex v and a curved line C. Figure 4(d) shows $d(v_k^D, C_I)$ uniquely defined as the one-way distance from a point of the target centerline to the source point. The source centerline C_I has many terminals that do not structurally correspond to those of the target centerline C_D because of its missing branches. In other words, the bronchial junctions or centerlines in the deflated state provide reliable landmarks for matching the two shapes, but the bronchial terminals in the inflated state should not be matched to those in the deflated state. These observations suggest that the one-way distance $C_D \to C_I$ enables evaluation of the validity of the distances corresponding to the visualized junctions and branches. In this scheme, the position of the bronchial terminal indicated by the dotted green arrow in Fig. 1(b) is spatially interpolated using reliable corresponding points obtained from the nearest surfaces, junctions, and centerlines with one-way correspondence.

Full objective

The discrete form of the objective function E can be described using the two distance measures as follows:

$$E = d_s(S_I, S_D)^2 + \alpha d_c(C_I, C_D)^2 + \beta \sum_{v_i \in M_I} \|L(u_i)\|^2, \qquad (5)$$

where α and β are the weights, u_i is the local displacement at vertex v_i, and $L(u_i)$ is the discrete Laplacian of the local displacement vector, described as

$$L(u_i) = \sum_{v_j \in A_i} \omega_{ij}(u_i - u_j). \qquad (6)$$

Here, ω_{ij} is the edge weight and A_i is the set of adjacent vertices of one ring connected by vertex v_i and the edges. As the discrete Laplacian approximates the mean curvature normal (Nealen et al., 2006), the third term in Eq. (5) makes the deformation field spatially smooth and diffeomorphic. Although there are several methods for calculating the weights, the general one is cotangent discretization based on the per-edge Voronoi areas. The deformation field u is obtained by iteratively updating v_i while minimizing E. The step-by-step update avoids local mismatches during the early stage if there is a considerable distance between the two models.

2.5. Contraction and rotational components

This section describes methods for analyzing the heterogeneity of the pneumothorax-associated deformation using the registered models. Figure 5(a) illustrates an ideal case of homogeneous deformation with zero rotational components. As the pulmonary hilum is physically fixed and not affected by pneumothorax-associated deformation, we use its position as the origin. In this case, the per-vertex displacement $u_i = \phi(v_i) - v_i$ towards the hilum corresponds to the local contraction component s_i, and we can estimate the local characteristics of the surface contraction using the size of u_i.

Figure 5(b) shows a real example of pneumothorax-associated lung deformation with rotation. The contraction was accompanied by various types of rotations, as observed in different subjects. As each subject was measured in the same right lateral position, we consider it unlikely that posture differences were the major cause of rotational variations. Rather, we consider that such rotations are caused by sliding motions between lobes and subject-specific physical interactions between the lobes and the thoracic cavity, such as friction and adhesion. Therefore, the rotational components can be regarded as external disturbance that does not reflect differences in the characteristics of lung tissue between subjects. As this study aimed to analyze the tissue characteristics of the lung lobes, rotational components caused by external factors were excluded from our analysis.

We employed simple calculation methods to extract the contraction component from the deformation field. In Fig. 5 (c), v_i and $\phi(v_i)$ are corresponding vertices of the initial model and the registered model determined by DMR, respectively. To extract contraction s_i from the displacement vector u_i, v_i' is defined as the position where the rotational component r_i is removed from $\phi(v_i)$. As the pulmonary hilum (i.e., the origin in this study) is supposed to be the center of rotation, the direction of the contraction component s_i is defined as the vector towards the hilum, as shown in Fig. 5(d). The contraction s_i and rotational component r_i are defined as Eq. (7) and (8), respectively.

$$s_i = \frac{|\phi(v_i)| - |v_i|}{|v_i|} v_i, \tag{7}$$

$$r_i = u_i - s_i. \tag{8}$$

2.6. Strain definition for bronchi and parenchyma

The objective of this study was to analyze the heterogeneity in pneumothorax-associated deformation of the lungs. For this purpose, the strains of bronchi and other parenchyma regions were compared according to the registered CT models. In general, strain is a measure of the displacement between particles in the body relative to a reference length. The Cauchy strain is defined as

$$\varepsilon = \frac{\Delta L}{L} \tag{9}$$

where L is the original length between two sampled points, and ΔL is the change in length between the sampled points in the deformed body. To compare the strains of anatomically corresponding
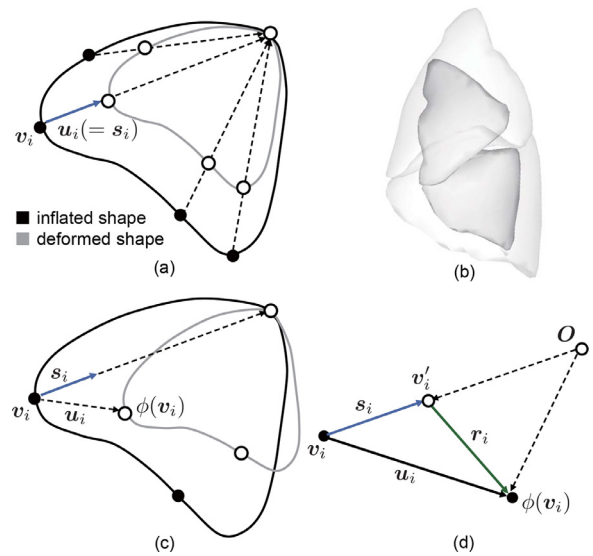

Fig. 5. Contraction and rotational components in pneumothorax-associated lung deformation. (a) Homogeneous deformation with zero rotational components, (b) a real example of pneumothorax-associated deformation with rotation, (c) the contraction component extracted from the deformation field, and (d) its geometrical description.
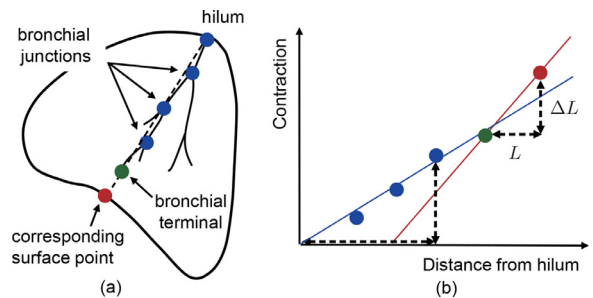

Fig. 6. Definition of the Cauchy strain for bronchi and parenchyma in each lobe. (a) The positional relationship between the hilum, bronchial junctions, and terminal and corresponding surface point. (b) 2D plots and strain calculation for bronchi (blue line) and parenchyma (red line). (For interpretation of the references to colour in this figure legend, the reader is referred to the web version of this article.)

structures, we divided the lung's internal structures into two regions: the bronchial region and the region between the bronchial terminal and the surface (notated as parenchyma in this paper). This latter region comprises microtissues such as alveoli and terminal bronchioles, and the structures are not clearly identifiable on CT imaging. To determine L and ΔL for the corresponding two regions, we focused on a set of spatially-continuous points per bronchial branch, bronchial terminal, and its extended point on the lung surface. Figure 6(a) shows the sampled points: the pulmonary hilum, three bronchial junctions (blue), the bronchial terminal (green), and corresponding surface point (red) obtained from one bronchial branch. The surface point is defined as the intersection of the straight line determined by the pulmonary hilum and the bronchial terminal. In this case, L is determined as the Euclidean distances of the two neighboring points in the deflated state and ΔL is the change in the distance that occurs in the deformation between the inflated state and the deflated state.

Figure 6 (b) illustrates a 2D plot representing the relation between the Euclidean distance between the pulmonary hilum $|v_i|$ and the contraction $|s_i|$ for the sampled points. Here, the gradient of the line defined by the two neighboring points represents the Cauchy strain for the local region. As we confirmed that the set of plots for one bronchial branch were mostly distributed linearly,
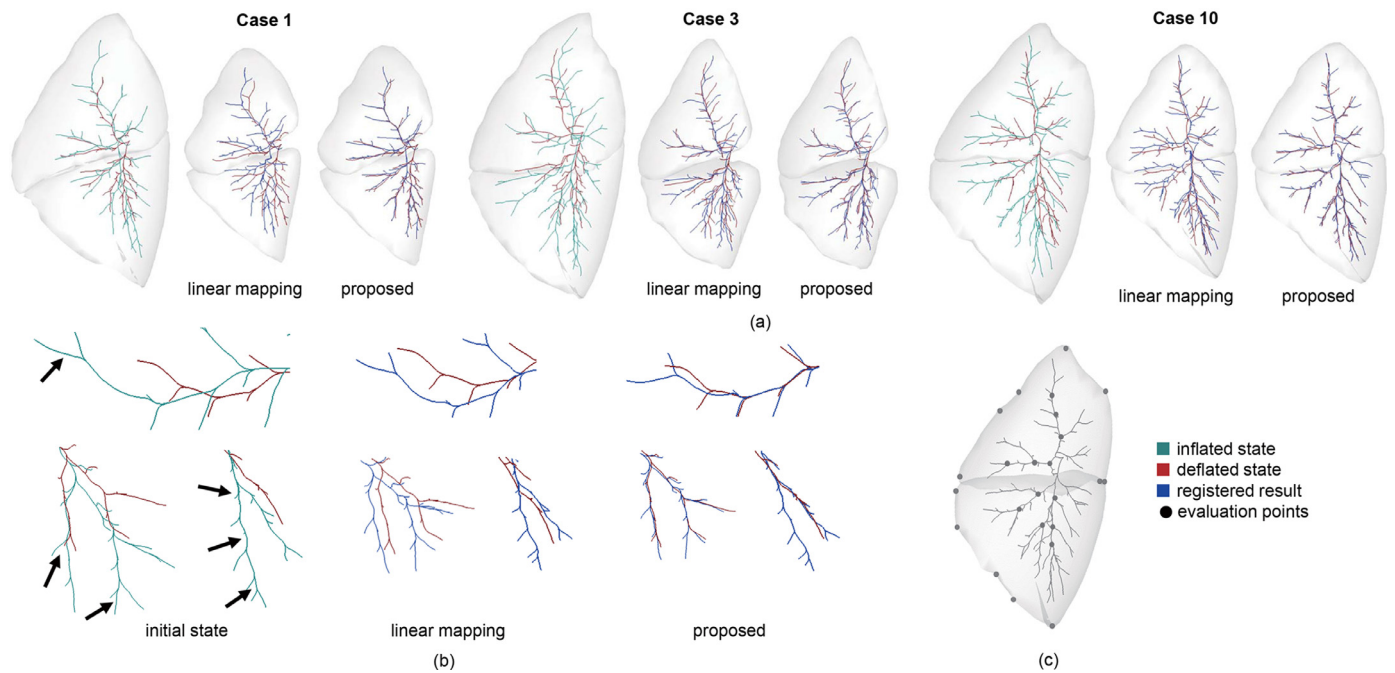
Fig. 7. Typical registration results with variations in bronchial anatomy and lobe deformation. (a) visual comparison between the proposed DMR and surface registration with linear mapping, (b) enlarged images of the local bronchial shapes, (c) 24 points for evaluating target registration error.

the strain for the bronchi was calculated from the linear regression of the plots from the bronchial junctions and the terminal, as shown by the blue line in Fig. 6(b). The strain for the region between the bronchial terminal and the lung surface was obtained from the gradient of the red line. In this study, reliable corresponding points are not always obtained from overall volumetric regions because of the low contrast images in the deflated lungs. Also, the deformation of parenchyma is locally affected by rotation or sliding motions between lobes, which makes analysis with a volumetric deformation map difficult. The proposed bronchial-tree-based strain analysis enables to compare corresponding bronchial centerlines and parenchyma on a one-to-one basis.

3. Experiments

In the experiments, the performance of the proposed DMR framework was first evaluated using ten in vivo lung models (Cases 1–10). The efficacy of the objective function was confirmed by comparing it with existing deformable mesh registration approaches. Then, the heterogeneity of the strains on the bronchus and parenchyma was investigated using the spatial displacement obtained from the registered models. The proposed DMR and deformation analysis methods were implemented using Visual C/C++ and OpenGL. A computer with a graphics processing unit (CPU: Intel Core i7 3.7GHz, Memory: 64 GB, GPU: NVIDIA GeForce GTX 1080) was used throughout the experiments.

For the weights in the developed framework, we used 1.0 for λ, the same value used in a previous study (Nakao et al., 2019). After examining several parameter sets, $(\alpha, \beta) = (2.0, 2.0)$ were used for the weight parameters in the objective function. For each registration step, when the minimum value of the objective function was not updated in the most recent 20 iterations, or when the number of updates reached 1000 times, the iterative update was terminated and the next registration step was initiated.

3.1. Quantitative comparison of DMR

In the first experiment, the registration accuracy was confirmed for the paired CT models with pneumothorax-associated deforma-

tion. The inflated lung models were deformed to the deflated target models and the differences between the deformed and target shapes were quantified using multiple shape similarity criteria. The mean distance and Hausdorff distance (Kim et al., 2015; Nakao et al., 2019) were used as measures of the shape similarity of the surfaces. The mean and maximum of the one-way point-to-point distances were used to measure the similarity of the bronchial centerlines. The Hausdorff distance measures the longest distance among the minimum point distances between two surfaces, whereas the mean distance is the average of the minimum point distances. The Hausdorff distance is a strict error metric as it measures the largest distance between two shapes.

Unlike segmentation or recognition problems, deformation analysis requires point-to-point correspondence between two shapes. The accuracy of the registered shape after DMR was validated by the target registration errors (TREs) on anatomical evaluation points of the lung surface and bronchial junctions. The TREs were defined as the Euclidean distances between the manually-placed evaluation points of the target (deflated) model and the deformed (registered) model generated from the inflated model. Automatic identification of the unique/distinctive features of individual models is difficult because their shapes comprise smooth curved surfaces and their bronchial tree structures vary substantially among patients (See Fig. 7). With the anatomical review of two expert surgeons, 12 evaluation points were manually set on the surfaces and bronchial junctions of the deflated models. The corresponding vertices of the inflated models were also determined. Fig. 7(c) shows an example of all 24 evaluation points for one subject. The evaluation points for the surfaces were selected from the ridge of the lung surface with large curvatures and locally similar features. As the bronchial tree structures were anatomically different between subjects, as shown in Table 1, the bronchial junctions were selected such that the correspondence between the inflated/deflated shapes was visually clear.

The proposed DMR was compared with the existing mesh-based registration methods:

- Affine transformation (AF)
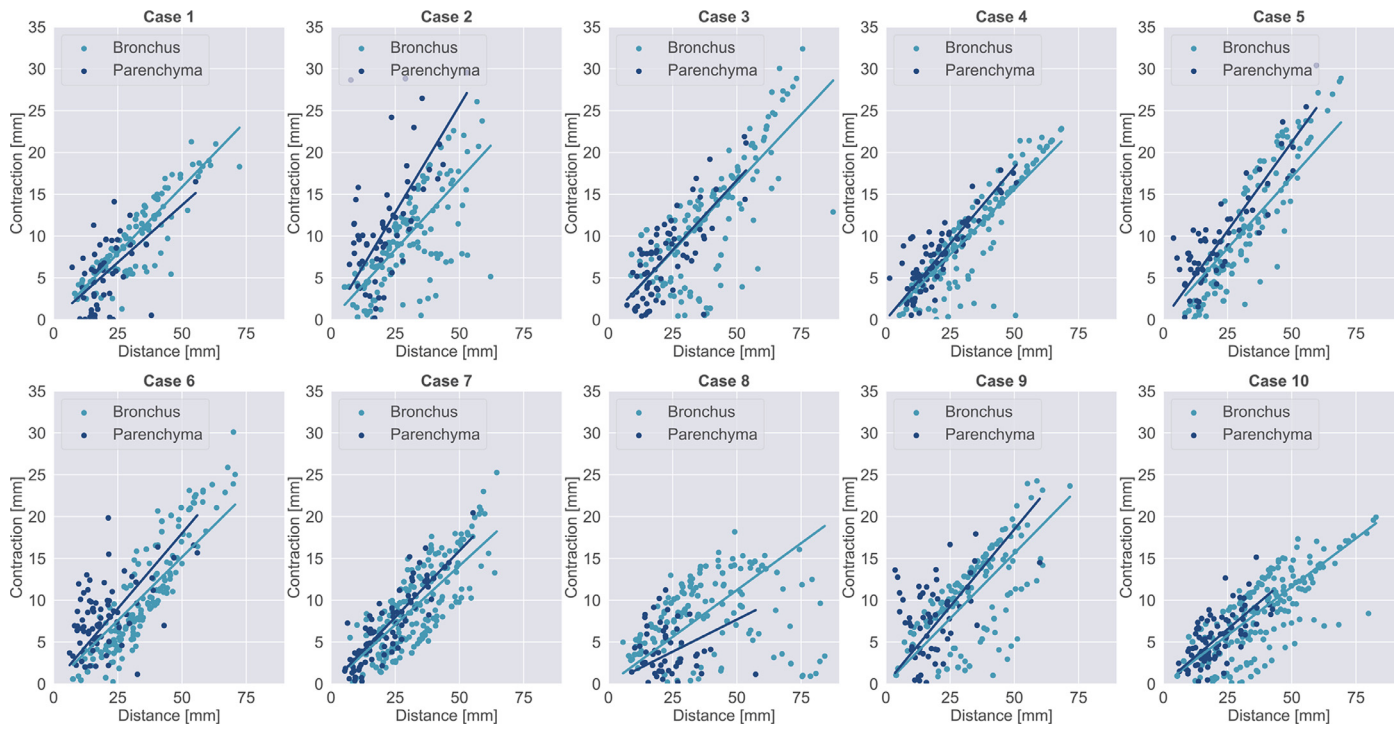- Piecewise affine transformation (PWA)

京都大学
KYOTO UNIVERSITY

A Self-archived copy in
Kyoto University Research Information Repository
https://repository.kulib.kyoto-u.ac.jp

京都大学学術情報リポジトリ
KURENAI 紅
Kyoto University Research Information Repository

Fig. 8. The relationship between the Euclidean distance from the pulmonary hilum and the contraction components for bronchi and parenchyma. The gradient of the regression line represents the strain.

Table 2
The mean ± standard deviation of DMR results for mean distance (MD), Hausdorff distance (HD), centerline distance (CD), and target registration errors (TREs) for surfaces and bronchial centerlines.

Error metric	Rigid	AF	PWA	LSM	Proposed
MD [mm]	10.09 ± 2.14	4.13 ± 1.22	1.49 ± 0.20	0.24 ± 0.05	0.24 ± 0.06
HD [mm]	29.65 ± 5.72	15.97 ± 4.84	6.35 ± 1.85	0.74 ± 0.18	0.78 ± 0.17
CD (mean) [mm]	4.08 ± 1.15	3.83 ± 1.80	3.88 ± 1.68	3.86 ± 1.70	1.51 ± 0.58*
CD (maximum) [mm]	11.48 ± 4.71	12.78 ± 6.61	12.07 ± 6.04	12.40 ± 6.14	7.53 ± 2.47*
TRE (surface) [mm]	22.91 ± 8.81	10.65 ± 5.46	6.11 ± 3.69	4.57 ± 4.13	4.55 ± 2.82
TRE (bronchus) [mm]	7.59 ± 4.77	5.63 ± 3.60	6.10 ± 3.54	6.14 ± 3.51	3.97 ± 2.75*
					*: p <0.01

- Laplacian-based shape matching (LSM)

The rigid registration result was also listed to confirm the initial difference and complexity of the inter-subject matching of collapsed lungs. PWA and LSM were investigated as an integrated registration framework to match the experimental conditions with those of the proposed method; for PWA and LSM, affine registration was first applied to globally match the posture and volume of the overall shape. Additionally, in the LSM, piecewise affine registration was performed in advance to achieve a globally stable and locally strict registration, similar to the proposed method. As these existing methods were originally applied to surface models, bronchial tree registration was performed with linear mapping, that is, the displacement of the bronchial structures was linearly interpolated from the deformed surfaces. In the PWA step, an axis-aligned bounding box was calculated for each lobe, and its space was divided into $4 \times 4 \times 4 = 64$ subspace. We note that the difference between the LSM and proposed method lies in the weight parameters $(\alpha, \beta) = (0.0, 2.0)$ used for the objective function in LSM. This setting also serves as confirmation of the role of the proposed one-way centerline distance.

Table 2 shows values of the error metrics obtained from the registration results of the 10 subjects. The mean distance (MD), Hausdorff distance (HD) for surfaces, the mean and maximum cen-

terline distance (CD), and target registration errors (TREs) for lung surface and bronchi are listed. The proposed DMR achieved significantly smaller CDs and TREs for bronchial centerlines compared with the conventional linear mapping (one-way analysis of variance, ANOVA; $p < .01$ significance level). There was no significant difference in MD, HD, and TRE for lung surfaces, which means that the proposed DMR outperformed the conventional linear mapping in matching bronchi with missing branches, while maintaining a similar registration quality for surfaces. Specifically, the small TREs of less than 5 mm demonstrate that spatial displacement analysis focusing on the difference between the lung's bronchi and parenchyma tissues is possible using the registered models.

Fig. 7 (a) shows typical registration results of three subjects (Cases 1, 3, and 10), which include variations in the large deformation with rotations and missing shapes in the bronchial structures. It can be visually confirmed that compared with the conventional method, the proposed DMR achieves smaller errors in matching bronchi. Fig. 7 (b) shows enlarged images of the local bronchial shapes for Cases 1 and 6. There are some missing shapes in the target bronchi, as indicated by the arrows. Point-to-point registration using only bronchial tree structures resulted in large registration errors including irregular bends and overfitting due to the underdetermined matching problem. In the proposed method, such errors or mismatching results were not confirmed in all sub-

Table 3

The mean ± standard deviation of strains for bronchus and parenchyma in pneumothorax-associated deformation .

Case	Bronchus	Parenchyma
1	0.315 ± 0.064	0.286 ± 0.194
2	0.372 ± 0.176	0.616 ± 0.506
3	0.320 ± 0.209	0.329 ± 0.162
4	0.275 ± 0.099	0.430 ± 0.398
5	0.247 ± 0.138	0.499 ± 0.330
6	0.230 ± 0.109	0.463 ± 0.239
7	0.250 ± 0.131	0.303 ± 0.138
8	0.295 ± 0.102	0.209 ± 0.159
9	0.350 ± 0.128	0.580 ± 0.640
10	0.255 ± 0.121	0.272 ± 0.118
Mean ± SD	0.292 ± 0.141	0.395 ± 0.296*
		*: $p < 0.05$

jects. The proposed objective function evaluates the deviation of both the surface and bronchial structures, and spatially-valid registration is performed, even for the target models with missing information.

3.2. Analysis of pneumothorax-associated deformation

The strains of the sampled points of the bronchi and parenchyma were investigated using the analysis method described in Section 2–6. As all bronchial branches were targeted, the number of branches was equal to the number of terminals N_t of the deflated model in Table 1. For each branch, the displacement vectors for the bronchial junctions, terminals, and corresponding surface points were obtained from the registered models, and the contraction component derived after removing irregular rotation was plotted.

Fig. 8 is a 2D plot showing the relationship between the reference distance and the contraction components for bronchi and parenchyma. The Euclidean distance from the pulmonary hilum was used for the reference distance of the bronchi, and the Euclidean distance from the bronchial terminal was used for the parenchyma. The number of plots in the graph equals the number of sampled points for all cases. The light and dark blue plots are the contractions of the bronchi and parenchyma, respectively. The gradients of the two regression lines represent the strains, which are characterized by the gradients in the parenchyma, and show 1) higher gradients for seven out of ten subjects, 2) slightly higher gradients for Case 3, and 3) lower gradients for the other two subjects.

Table 3 shows the mean strain for the bronchi and parenchyma region in the ten subjects. The mean values were computed from the strains of the sampled points in Fig. 8. The means ± standard deviation of the strains in the bronchus and lung parenchyma were 0.292 ± 0.141 and 0.395 ± 2.96, respectively. The strain of the lung parenchyma was higher than that of the bronchi, except for Cases 1 and 8. A significant difference was found between the two regions (ANOVA; $p < .05$ significance level), with the mean value of the parenchyma region being 35% higher.

We visualized the deformation fields to further investigate the reasons why such different characteristics appeared in the strains. Fig. 9 shows the visualization results of the displacements, contractions, and rotational components obtained from Cases 1, 3, 5, and 8. In Cases 1 and 8, the strain in the parenchyma is lower than that in the bronchi. In Case 3, the strains of the two regions are similar. Case 5 is typical, with a large deformation and strain in the parenchyma higher than that in bronchi. The displacement vectors

represent the corresponding points of the inflated/deflated models and the colors show the magnitude of the displacements.

The visualization results demonstrate the following points:

- Rotational directions in upper and lower lobes were different, resulting in physical interactions and the occurrence of spaces among the lobes in Cases 1 and 3.
- In Case 5, both the upper and lower lobes deformed while preserving their shape features and relative postures.
- Deformation of the lower lobe in Case 8 was unique and was strongly affected by external forces from the diaphragm.

We further discuss these influences on the strain analysis in the next section.

4. Discussion

To our knowledge, this study is the first to analyze pneumothorax-associated deformation of overall shape of the lungs including all lobes and bronchial tree structures using paired CT images measured in the same posture. Deformable registration methods were designed for inflated/deflated lung models, and non-linear mapping between the lung parenchyma and bronchi was obtained. While other studies have targeted pneumothorax-associated deformation, the main focus of their analyses was limited to either the lung surface or the bronchus region. A recent study (Lesage et al., 2020) used CT data of six patients with pneumothorax after lung biopsy and chest tube insertion, and reported preliminary results for predicting the performance of deflated lung surfaces using a hyperelasitic finite-element model. Our previous study (Nakao et al., 2019) also focused on surface deformation of collapsed lungs.

In the deformation analysis, strains in each region of the lung parenchyma and bronchi were calculated and a significant difference was found between the two strains. The mean strain of the parenchyma was higher than that of the bronchi, although considerable deviations in the values were found between subjects. In Case 3, the two regions showed similar strains, whereas Cases 1 and 8 showed the opposite trend, with the strain in the bronchi being higher than that in the parenchyma. The visualization results of the deformation fields in Fig. 9 demonstrated that Cases 1 and 3 showed opposite rotational directions between the lobes. In this situation, the two lobes made contact with each other and physical interaction could not be ignored. Although rotational components were found in other subjects, as shown in Case 5, the interaction between the lobes was observed to be small. Case 8 showed a unique deformation that was strongly affected by the diaphragm shape. We could not find the cause of this from the CT images, but soft tissue adhesion or biased forces from a ventilator might have acted on the lower lobe. The widely dispersed 2D plots in Fig. 8 suggest that the deformation in Case 8 contains outlying values with very small deformations or almost fixed points. We consider that these physical conditions influenced the natural contraction characteristics resulting in an error factor in the strain analysis of the three cases.

This paper targeted the left lung to measure stable pneumothorax-associated deformation in a limited number of live dogs. In the right lung, the physical interaction between the three lobes (upper, middle, and lower) may be more complicated than that in the left lung, although the same measurement protocol and registration algorithms could be applied to the right lung. In our experiments, the imaging data were only collected from 11 subjects, and further acquisitions were difficult because of renovations being performed to our animal experiment facilities. Further analysis of the non-linear characteristics of both left and right deformed lungs would be interesting.
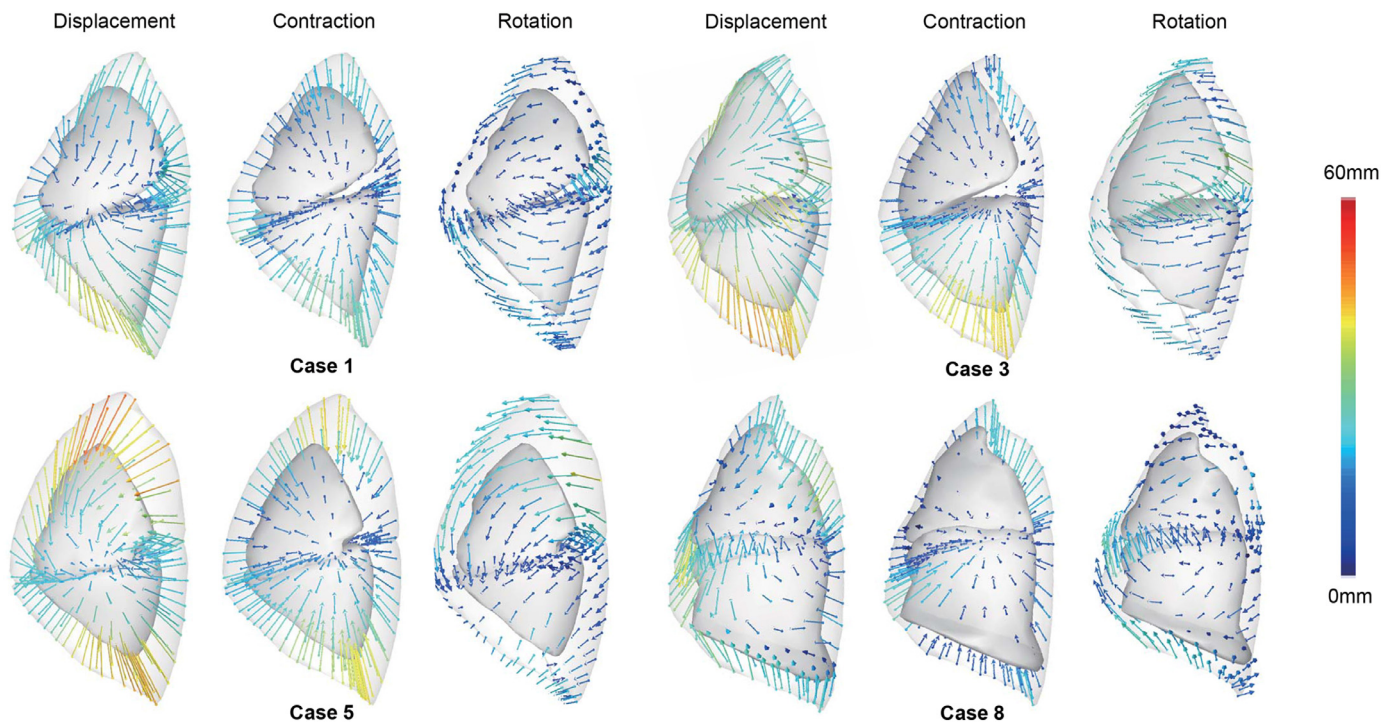
Fig. 9. Visualization results of four deformation fields, contractions, and rotational components. The displacement vectors represent the corresponding points of the inflated/deflated models. The colors show the magnitude of the displacements.

We assume that the clinical application of the proposed DMR techniques would be construction of a statistical deformation model representing the various pneumothorax states of the lung. Non-invasive intraoperative localization of tumors or nodules, especially those located deeper in the lungs, is desirable. The statistical deformation model could be used as prior knowledge to predict pneumothorax states in video-assisted thoracoscopic surgery (Wu et al., 2019). Because CT imaging is not generally available during surgery, it will be challenging to construct a patient-specific image database of collapsed lungs in the intraoperative condition. However, we have begun to analyze intraoperative deformation using CBCT images (Maekawa et al., 2020; Nakao et al., 2021a). Despite the limited measurement area, CBCT imaging is clinically feasible and will be useful for modeling intraoperative pneumothorax-associated deformations in real patients.

5. Conclusion

In this paper, we introduced a complete deformable mesh registration solution for mapping the lung's surface and bronchial structures including missing shapes, and analyzed the heterogeneity of pneumothorax-associated deformations using ten paired CT images of the lungs of Beagle dogs. The proposed DMR framework achieved stable registration with a Hausdorff distance error of less than 1 mm and a target registration error of less than 5 mm. Our results show that spatial deformation of the collapsed lung was heterogeneous. The means $\pm$ standard deviation of the strains in the bronchi and lung parenchyma were 0.292 ± 0.141 and 0.395 ± 2.96, respectively, with the mean value of the parenchyma region being 35% higher. We believe that the registered models and findings are suitable for statistical lung modeling and intraoperative tumor localization. Deformable registration of topological features with incomplete correspondence will have other important clinical applications, such as registration of CBCT images with partial organ shapes.

Declaration of Competing Interest

The authors declare that they have no known competing financial interests or personal relationships that could have appeared to influence the work reported in this paper.

CRediT authorship contribution statement

Megumi Nakao: Conceptualization, Methodology, Software, Writing – original draft. **Kotaro Kobayashi:** Methodology, Visualization. **Junko Tokuno:** Data curation, Investigation. **Toyofumi Chen-Yoshikawa:** Data curation, Validation, Resources. **Hiroshi Date:** Resources, Supervision. **Tetsuya Matsuda:** Supervision, Validation, Writing – review & editing.

References

Alvarez, P., Chabanas, M., Rouzé, S., Castro, M., Payan, Y., Dillenseger, J.-L., 2018. Lung deformation between preoperative CT and intraoperative CBCT for thoracoscopic surgery: a case study. SPIE Med. Imag. 10576, 7.

Wu, S., Nakao, M., Tokuno, J., Chen-Yoshikawa, T., Matsuda, T., 2019. Reconstructing 3D lung shape from a single 2D image during the deaeration deformation process using model-based data augmentation. IEEE EMBS International Conference on Biomedical and Health Informatics (BHI) 1–4.

Antiga, L., Steinman, D. A., 2011. The vascular modeling toolkit. http://www.vmtk.org/.

Beg, M.F., Miller, M.I., Trouvé, A., Younes, L., 2005. Computing large deformation metric mappings via geodesic flows of diffeomorphisms. Int. J. Comput. Vision 61 (2), 139–157.

Ehrhardt, J., Werner, R., Schmidt-Richberg, A., Handels, H., 2011. Statistical modeling of 4D respiratory lung motion using diffeomorphic image registration. IEEE Trans Med Imag. 30 (2), 251–265.

Fuerst, B., Mansi, T., Carnis, F., Sälzle, M., Zhang, J., Declerck, J., Boettger, T., Bayouth, J., Navab, N., Kamen, A., 2015. Patient-specific biomechanical model for the prediction of lung motion from 4-D CT images. IEEE Trans. Med. Imag. 34 (2), 599–607.

Gunay, G., Ha, L.M., Walsum, T.v., Klein, S., 2016. Semi-automated registration of pre- and intra-operative liver CT for image-guided interventions. SPIE Medical Imaging 9784, 8.

Heiselman, J.S., Collins, J.A., Clements, L.W., Weis, J.A., Simpson, A.L., Geevarghese, S.K., Kingham, T.P., Jarnagin, W.R., Miga, M.I., 2018. Technical note: nonrigid registration for laparoscopic liver surgery using sparse intraoperative data. SPIE Medical Imaging 10576.

Ilegbusi, O.J., Li, Z., Seyfi, B., Min, Y., Meeks, S., Kupelian, P., Santhanam, A.P., 2012. Modeling airflow using subject-specific 4DCT-based deformable volumetric lung models. Int J Biomed Imaging 2012, 350853.

Jud, C., Giger, A., Sandkühler, R., Cattin, P.C., 2017. A localized statistical motion model as a reproducing kernel for non-rigid image registration. Medical Image Computing and Computer-Assisted Intervention (MICCAI) 261–269.

Kazhdan, M., Bolitho, M., Hoppe, H., 2006. Poisson surface reconstruction. In: Proceedings of the fourth Eurographics symposium on Geometry processing. Eurographics Association, 1281965, pp. 61–70.

Kenngott, H.G., Wagner, M., Gondan, M., Nickel, F., Nolden, M., Fetzer, A., Weitz, J., Fischer, L., Speidel, S., Meinzer, H.P., Bockler, D., Buchler, M.W., Muller-Stich, B.P., 2014. Real-time image guidance in laparoscopic liver surgery: first clinical experience with a guidance system based on intraoperative CT imaging. Surg Endosc 28 (3), 933–940.

Kim, J., Valdes-Hernandez Mdel, C., Royle, N.A., Park, J., 2015. Hippocampal shape modeling based on a progressive template surface deformation and its verification. IEEE Trans. Med. Imag. 34 (6), 1242–1261.

Klein, S., Staring, M., Murphy, K., Viergever, M.A., Pluim, J.P., 2010. Elastix: a toolbox for intensity-based medical image registration. IEEE Trans. Med. Imag. 29 (1), 196–205.

Koo, B., Özgür, E., Le Roy, B., Buc, E., Bartoli, A., 2017. Deformable registration of a preoperative 3D liver volume to a laparoscopy image using contour and shading cues. Medical Image Computing and Computer Assisted Intervention 326–334.

Lesage, A.C., Rajaram, R., A, L.T., Rigaud, B., K, K.B., D, C.R., Cazoulat, G., 2020. Preliminary evaluation of biomechanical modeling of lung deflation during minimally invasive surgery using pneumothorax computed tomography scans. Phys Med Biol 65 (22), 225010.

Maekawa, H., Nakao, M., Mineura, K., Chen-Yoshikawa, T., Matsuda, T., 2020. Model-based registration for pneumothorax deformation analysis using intraoperative cone-beam CT images. 42nd Annual International Conference of the IEEE Engineering in Medicine & Biology Society (EMBC) 5818–5821.

Naini, A.S., Pierce, G., Lee, T.Y., Patel, R.V., Samani, A., 2011. CT Image construction of a totally deflated lung using deformable model extrapolation. Med Phys 38 (2), 872–883.

Nakamoto, M., Aburaya, N., Sato, Y., Konishi, K., Yoshino, I., Hashizume, M., Tamura, S., 2007. Thoracoscopic surgical navigation system for cancer localization in collapsed lung based on estimation of lung deformation. Med Image Comput Comput Assist Interv 10 (Pt 2), 68–76.

Nakao, M., Maekawa, H., Mineura, K., Chen-Yoshikawa, T., Matsuda, T., 2021. Kernel-based modeling of pneumothorax deformation using intraoperative cone-beam CT images. SPIE Medical Imaging 11598.

Nakao, M., Minato, K., 2010. Physics-based interactive volume manipulation for sharing surgical process. IEEE Trans. Info. Tech. Biomed. 14 (3), 809–816.

Nakao, M., Nakamura, M., Mizowaki, T., Matsuda, T., 2021. Statistical deformation reconstruction using multi-organ shape features for pancreatic cancer localization. Med Image Anal 67, 101829.

Nakao, M., Tokuno, J., Chen-Yoshikawa, T., Date, H., Matsuda, T., 2019. Surface deformation analysis of collapsed lungs using model-based shape matching. Int. J. Comput. Assist. Radiol. Surg. 14 (10), 1763–1774.

Nealen, A., Igarashi, T., Sorkine, O., Alexa, M., 2006. Laplacian mesh optimization. Proc. of 4th Int. Conf. on Computer Graphics and Interactive Techniques 381–389.

Nickel, F., Kenngott, H.G., Neuhaus, J., Andrews, N., Garrow, C., Kast, J., Sommer, C.M., Gehrig, T., Gutt, C.N., Meinzer, H.P., Muller-Stich, B.P., 2018. Computer tomographic analysis of organ motion caused by respiration and intraoperative pneumoperitoneum in a porcine model for navigated minimally invasive esophagectomy. Surg Endosc 32 (10), 4216–4227.

Oh, S., Kim, S., 2017. Deformable image registration in radiation therapy. Radiat Oncol J 35 (2), 101–111.

Rühaak, J., Polzin, T., Heldmann, S., Simpson, I.J.A., Handels, H., Modersitzki, J., Heinrich, M.P., 2017. Estimation of large motion in lung CT by integrating regularized keypoint correspondences into dense deformable registration. IEEE Trans. Med. Imag. 36 (8), 1746–1757.

Sadeghi-Naini, A., Shirzadi, Z., Samani, A., 2012. Towards modeling tumor motion in the deflated lung for minimally invasive ablative procedures. Comput Aided Surg 17 (5), 211–220.

Sotiras, A., Davatzikos, C., Paragios, N., 2013. Deformable medical image registration: a survey. IEEE Trans. Med. Imag. 32 (7), 1153–1190.

Tokuno, J., Chen-Yoshikawa, T.F., Nakao, M., Matsuda, T., Date, H., 2020. Resection process map: a novel dynamic simulation system for pulmonary resection. J Thorac Cardiovasc Surg 159 (3), 1130–1138.

Uneri, A., Nithiananthan, S., Schafer, S., Otake, Y., Stayman, J.W., Kleinszig, G., Sussman, M.S., Prince, J.L., Siewerdsen, J.H., 2013. Deformable registration of the inflated and deflated lung in cone-beam CT-guided thoracic surgery: initial investigation of a combined model- and image-driven approach. Med Phys 40 (1), 017501.

Wagner, M., Gondan, M., Zollner, C., Wunscher, J.J., Nickel, F., Albala, L., Groch, A., Suwelack, S., Speidel, S., Maier-Hein, L., Muller-Stich, B.P., Kenngott, H.G., 2016. Electromagnetic organ tracking allows for real-time compensation of tissue shift in image-guided laparoscopic rectal surgery: results of a phantom study. Surg Endosc 30 (2), 495–503.

Wilms, M., Ha, I.Y., Handels, H., Heinrich, M.P., 2016. Model-based regularisation for respiratory motion estimation with sparse features in image-guided interventions. Medical Image Computing and Computer-Assisted Intervention – MICCAI 2016 89–97.